Supplementary material: Single crystal diffraction study of $Ba[H_4C_4O_{10}][H_3C_4O_{10}][H_2CO_3][HCO_3]$, a hydrous mixed sp^2/sp^3-carbonate

Dominik Spahr*[,a], Elena Bykova[a], Lkhamsuren Bayarjargal[a], Victor Milman[b], Hanns-Peter Liermann[c], Björn Winkler[a]

[a]*Goethe University Frankfurt, Institute of Geosciences, Altenhöferallee 1, 60438 Frankfurt, Germany*
[b]*Dassault Systèmes BIOVIA, 22 Cambridge Science Park, Cambridge CB4 0FJ, United Kingdom*
[c]*Deutsches Elektronen-Synchrotron DESY, Notkestrasse 85, 22607 Hamburg, Germanyy*

1. Methods

1.1. Sample material

We used hydrothermal a synthesis to obtain $Ba[CO_3]$ single crystals, derived from an approach established for other carbonates.[1] The crystals were grown using barium chloride dihydrate ($BaCl_2 \cdot 2H_2O$) and ammonium bicarbonate (NH_4HCO_3) as starting materials according to the reaction:

$$BaCl_2 \cdot 2H_2O + 2NH_4HCO_3 \rightarrow BaCO_3 \downarrow + 2NH_4Cl + CO_2 \uparrow + 3H_2O \quad (1)$$

First, 1.5 mmol of analytical grade $BaCl_2 \cdot 2H_2O$ (99.99% purity, Merck, Darmstadt, Germany) was dissolved in 12.5 ml bidistilled water under magnetic stirring at ambient temperature. In addition, 1 mmol of ammonium bicarbonate, NH_4HCO_3 (99.99% purity, Merck, Darmstadt, Germany) was dissolved separately in 25 ml bidistilled water. Afterwards, the resulting solutions were mixed under magnetic stirring at room temperature and the resulting suspension transferred into a 60 ml Teflon cup. The Teflon cup was filled up to 50% of its volume. It was placed in a stainless steel autoclave and heated up to 503(1) K in two hours. The temperature was kept for 24 h. Afterwards, the oven was cooled down in two steps: First from 503(1) K to 453(1) K in 48 h and secondly from 453(1) K to 300(1) K in 24 h. The precipitate was obtained by vacuum filtration, washed with distilled water, and dried in an oven at 333(1) K. We obtained colorless crystals with a variety of crystal habits with edge lengths up to of 200 µm.

We used the CO_2 gas for the gas-jet (Nippon gases, purity $\geq$ 99.995%) and the argon purge gas (Nippon gases, purity $\geq$ 99.999%) as purchased.

1.2. High-pressure experiments

The high-pressure experiments were carried out using Boehler-Almax type diamond anvil cells (DACs) with 300 µm culet size and diamonds with 70° opening angle on both sides.[2] We used Re-gaskets which were pre-indented to a thickness of $\approx$ 45 µm. Gasket-holes with $\approx$ 100 µm diameter were drilled by a custom-built laser setup. A $Ba[CO_3]$ crystal with dimensions of $\approx 70 \times 30 \times 20$ µm^3 and a ruby chip for pressure determination were placed in the gasket hole on the bottom diamond (Fig. S 1 a). In addition, we added a piece of pure Re-metal ($\approx$ 10 µm) on the bottom diamond for the alignment of the X-ray beam (Fig. S 1 a). The pressure was determined by measuring the shift of the ruby fluorescence and we assume an error of 6% due to non-hydrostatic conditions.[3] We expect that the pressure conditions in the DAC before laser-heating are very likely non-hydrostatic as CO_2-III may sustain pressure gradients up to 0.2 GPa µm^{-1} at high pressures without heating.[4]

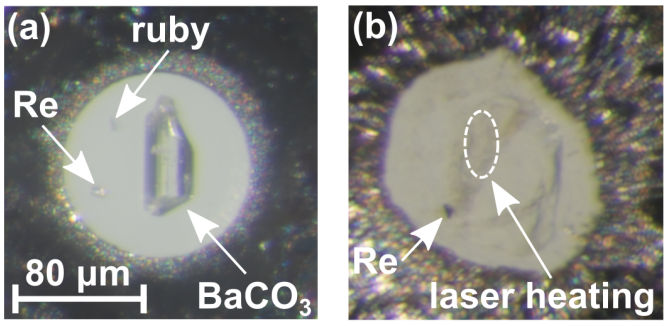

Figure S 1: (a) $Ba[CO_3]$ crystal, ruby chip and Re-metal piece in the gasket hole, placed on the bottom diamond before the cryogenic CO_2-loading. (b) The $Ba[CO_3]$ + CO_2 (+ H_2O) mixture after laser heating at 40(3) GPa up to temperatures of $\approx 2000(300)$ K.

Afterwards, CO_2 dry-ice was directly condensed into the gasket hole using a custom-built cryogenic loading system (see Spahr et al.[5]) derived from an earlier concept.[6] The DAC was opened and placed on a liquid nitrogen cooled Cu-holder. It was cooled down to $\approx$ 100 K. Ar (10 l min^{-1}) was used as a purge-gas to avoid the precipitation of H_2O ice. We assume that small amounts of H_2O were inadvertently co-condensed from the residual moisture in the CO_2- or Ar-gas. We used a small nozzle to align a CO_2 gas jet with 5 l min^{-1} directly on the gap between upper diamond and the gasket. The precipitation of the CO_2 in the gasket hole was monitored by an optical microscope and a camera. After a sufficient amount of CO_2 was gathered in the gasket hole, the DAC was tightly closed. Finally, the DAC was compressed to the target pressure without intermediate heating and heated up to maximum temperatures of $\approx 2000(300)$ K of 40(3) GPa (Fig. S 1 b).

*d.spahr@kristall.uni-frankfurt.de

1.3. Laser heating

Double-sided laser-heating was performed with a custom-built laser setup using a Coherent Diamond K-250 pulsed CO_2 laser ($\lambda = 10600$ nm).[7] The laser power was adjusted to achieve a coupling of the laser to the sample from both sides (1–3 W) and the focusing on the sample results in a heating area of $\approx 30 \times 50$ μm^2. The highest temperature achieved during the laser heating was $T_{max} \approx 2000(300)$ K. The temperatures were determined by the two-color pyrometer method, employing Planck and Wien fits.[8] The heating time was ≈ 60 minutes. It is well established that laser-heating in DACs always suffers from large temperature gradients and the actual temperature is strongly dependent on the coupling of the laser with the sample, especially at lower temperatures. We estimate an uncertainty of at least $\pm$15% of the nominal temperature in the laser-heated region depending on the focus of the laser beam, based on typical 2D temperature-gradient determination experiments performed in DACs.[9]

1.4. Single crystal synchrotron X-ray diffraction

Single crystal synchrotron X-ray diffraction was carried out at PETRA III (DESY) in Hamburg, Germany, at the extreme conditions beamline P02.2.[10] The beam size on the sample was 2.0 (H) $\times$ 2.0 (V) μm^2 (FWHM), focused by Kirkpatrick Baez mirrors. The diffraction data were collected using a Perkin Elmer XRD1621 detector, a wavelength of 0.2899 Å (42.7 keV) and a detector to sample distance of 396 mm, calibrated using the powder diffraction of a CeO_2 standard and the software DIOPTAS.[11] We rotated the DAC by $\pm 34^\circ$ around the axis perpendicular to the beam while collecting frames in 0.5° steps with 4 s acquisition time per frame. The diffractometer/detector geometry was calibrated using diffraction data collected from a single crystal of enstatite in a DAC.

Before the single crystal data collection, the synchrotron X-ray beam was centered on the small Re-piece to ensure a very good adjustment of the rotation axis. We collected X-ray powder diffraction on regularly spaced grid points using the μm-sized X-ray beam, to locate a suitable region for subsequent single crystal X-ray diffraction experiments. After the data collection of the single crystal X-ray diffraction experiments, the reflections were indexed and integrated employing CrysAlis^{PRO} (version 43.67a).[12] We used the Domain Auto Finder program (DAFi) to find possible single crystal domains for the subsequent data reduction.[13] The structure solution and refinement were performed using the software package OLEX2 employing SHELXT for the crystal structure determination and SHELXL for the refinement.[14–16]

1.5. Density functional theory-based calculations

First-principles calculations were carried out within the framework of density functional theory (DFT), employing the Perdew-Burke-Ernzerhof (PBE) exchange-correlation functional and the plane wave/pseudopotential approach implemented in the CASTEP simulation package.[17–19] "On the fly" norm-conserving or ultrasoft pseudopotentials generated using the descriptors in the CASTEP data base were employed in conjunction with plane waves up to a kinetic energy cutoff of 1020 eV or 630 eV, for norm-conserving and ultrasoft pseudopotentials, respectively. The accuracy of the pseudopotentials is well established.[20] A Monkhorst-Pack grid was used for Brillouin zone integrations.[21] We used a distance between grid points of <0.023 Å^{-1}. Convergence criteria for geometry optimization included an energy change of $<5 \times 10^{-6}$ eV atom^{-1} between steps, a maximal force of <0.008 eV Å^{-1} and a maximal component of the stress tensor <0.02 GPa. Phonon frequencies were obtained from density functional perturbation theory (DFPT) calculations.[22,23] Raman intensities were computed using DFPT with the "$2n+1$" theorem approach.[24] A correction scheme for van der Waals (v.d.W.) interactions was applied for the calculations used to quantify the compression behaviour. We employed the correction scheme developed by Tkatchenko and Scheffler.[25]

2. Results

2.1. Structure of $Ba[H_4C_4O_{10}][H_3C_4O_{10}][H_2CO_3][HCO_3]$

The analysis of our experimental diffraction data shows that several phases are present after the laser-heating and that the measured crystal was part of a multi-grain reaction product. We solved the crystal structure of $Ba[H_4C_4O_{10}][H_3C_4O_{10}][H_2CO_3][HCO_3]$ in the triclinic space group $P1$ (No. 1) with $Z = 1$ and a R-value of 6%. Table S 1 lists the crystallographic parameters from the single crystal structure solution valid for 40(3) GPa in comparison to v.d.W. corrected DFT calculations. The unit cell parameters of the experimental and theoretical structural model match within the expected errors.

Table S 1: Structural parameters of the mixed sp^2/sp^3 barium hydrogencarbonate $Ba[H_4C_4O_{10}][H_3C_4O_{10}][H_2CO_3][HCO_3]$ at 40(3) GPa from single crystal structure solution (ambient temperature) in triclinic space group $P1$ in comparison to theoretical data derived from DFT calculations (athermal limit).

	Single Crystal	DFT
Crystal data		
Crystal system	Triclinic	
Space group	$P1$	
Chemical formula	$BaC_{10}O_{26}H_{10}$	
M_r	683.52	
a (Å)	6.346(2)	6.4017
b (Å)	6.377(2)	6.3755
c (Å)	8.191(2)	8.2238
α (°)	89.77(2)	89.23
β (°)	89.66(2)	90.24
γ (°)	60.72(4)	60.20
V (Å^3)	289.1(2)	291.21
Z	1	1
Data collection		-
F_{000}	334	-
θ range (°)	1.80–17.53	-
measured reflections	4537	-
independent reflections	1097	-
reflections $I > 2\sigma(I)$	886	-
R_{int}	0.021	-
		-
Refinement		-
$R[F > 2\sigma(F)]$, $wR(F)$	0.060, 0.151	-
No. of reflections	1097	-
No. of parameters	161	-
No. of restraints and constraints	384	-
$\Delta\rho_{max}$, $\Delta\rho_{min}$ (e Å^{-3})	0.80, -0.66	-

A refinement of the site occupancies of the two barium positions resulted in occupancy values very close to 2/3 and 1/3. Therefore, for the further refinements the occupancy parameters of the barium positions were fixed. All non-hydrogen atoms were refined anisotropically. In order to account for the pseudo-hexagonal symmetry and to improve the data/parameter ratio, the thermal displacement parameters of the carbon and oxygen atoms, which would be identical in $P\bar{3}$ space group symmetry, were constrained to be equal. All hydrogen atoms were refined isotropically and the hydrogen positions were refined with a "riding model" and $U_{iso}(H) = 1.5U_{iso}(O)$. The O–H bonds were allowed to rotate and the initial hydrogen positions were taken from the DFT-calculations. In addition, soft constraints for the C–O bond distances (with a tolerance of 0.05–0.1 Å) have been introduced, to constrain the distances which would be identical in $P\bar{3}$ space group symmetry. Furthermore, the structure was refined as a 4-component inversion twin to account for the hexagonal pseudo-symmetry.

Due to the pseudo-symmetry the *PLATON*/checkCIF program suggests $P\bar{3}$ as a new space group with a 100% fit of 3-fold axis by testing the triclinic structural model.[26] Nevertheless, our DFT calculations failed to converge to a reasonable structural model in higher space group symmetries than $P1$. This is a result of the symmetry constraints for the hydrogen positions in higher space group symmetries. A comparison between the experimental structural model and the one derived from the DFT calculations ("option 1") is shown in Figure S 2.

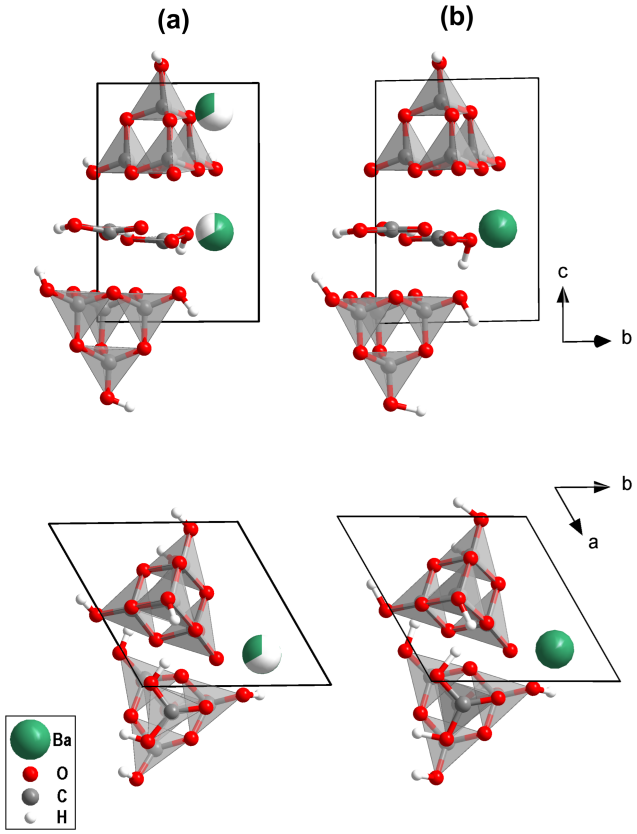

Figure S 2: (a) Experimental structural model from single crystal structure solution at 40(3) GPa and (b) DFT-calculated ("option 1") structural model of $Ba[H_4C_4O_{10}][H_3C_4O_{10}][H_2CO_3][HCO_3]$ at 40 GPa viewed along the a-axes (top) and along the c-axes (bottom). Partially filled spheres indicate partial site occupancies of barium. CCDC: 2332909 (exp.) and 2332910 (DFT).

Figure S 3 shows a $2 \times 2 \times 2$ super cell of the crystal structure of $Ba[H_4C_4O_{10}][H_3C_4O_{10}][H_2CO_3][HCO_3]$ at 40 GPa derived from DFT-based geometry optimizations. In order to mimic the Ba-disorder, one Ba atom was placed on the "option 2" position, while all others were located on the "option 1" position.

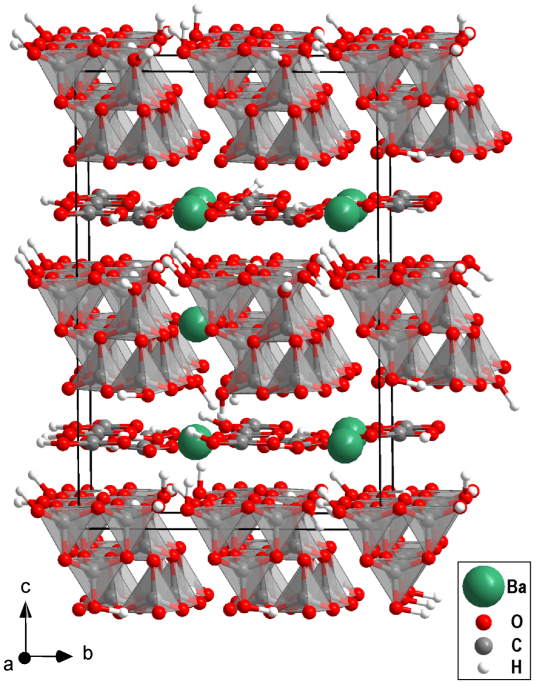

Figure S 3: $2 \times 2 \times 2$ super cell of the crystal structure of $Ba[H_4C_4O_{10}][H_3C_4O_{10}][H_2CO_3][HCO_3]$ from DFT calculations at 40 GPa, showing the layers of $[H_4C_4O_{10}]$-/$[H_3C_4O_{10}]^-$-groups and $[H_2CO_3]$-/$[HCO_3]^-$-groups (CCDC: 2332911).

Table S 2 lists the interatomic distances and angles between the barium atom and the oxygen/hydrogen atoms in the structural model derived from the DFT calculations ("option 1") at 40 GPa. The Ba–O distances range from 2.45 Å to 2.78 Å. The O–H bond distances are ≈ 1 Å, while the shortest Ba–H contact is 2.45 Å.

Table S 2: Interatomic distances and angles between the barium atom and the oxygen/hydrogen atoms in the structure of $Ba[H_4C_4O_{10}][H_3C_4O_{10}][H_2CO_3][HCO_3]$ at 40 GPa in triclinic space group $P1$ from DFT calculations (athermal limit).

atom 1	atom 2	$d_{1,2}$ (Å)	atom 3	$d_{2,3}$ (Å)	$\theta_{1,2,3}$ (°)
Ba	O10A	2.781	H10A	0.997	124.6
Ba	O8A	2.715	H8A	1.010	66.1
Ba	O9A	2.635	H9A	0.992	103.6
Ba	O9B	2.590	H9B	1.012	78.1
Ba	O10B	2.568	H10B	1.004	107.3
Ba	O52A	2.566	H53B	1.025	106.8
Ba	O51A	2.563	H51A	1.006	111.5
Ba	O51B	2.563	H51B	1.013	72.1
Ba	O53B	2.584	-	-	-
Ba	O8B	2.542	-	-	-
Ba	O53A	2.527	-	-	-
Ba	O53B	2.452	-	-	-

Table S 3 lists the nearest Ba–H contacts in the DFT-based structural model. The closest contact between a barium and a hydrogen atom is ≈ 2.483 Å for the "option 1" model calculated at 40 GPa. We are aware that some short Ba–H contacts are present in the experimental structural model such as Ba1–H10A (≈ 1.91 Å), Ba1–H9B (≈ 1.75 Å) or Ba2–H51B (≈ 2.09 Å), which are not present in the DFT-calculated structural data. We would like to stress here, that due to the presence of the heavy barium atoms the experimentally determined hydrogen positions are somewhat uncertain, which causes some close Ba-H-O contacts the experimental structural model. In contrast, it is generally accepted that DFT calculations provide accurate hydrogen positions.[27] This is in agreement with the nearest Ba–H contacts in the calculated model (Table S 3), where no contacts < 2.4 Å are present.

Table S 3: Nearest Ba–H contacts in the DFT-based structural model of $Ba[H_4C_4O_{10}][H_3C_4O_{10}][H_2CO_3][HCO_3]$ at 40 GPa in triclinic space group $P1$ (athermal limit).

atom 1	atom 2	$d_{1,2}$ (Å)
Ba2	H8A	2.483
Ba2	H9B	2.580
Ba2	H52B	3.023
Ba2	H53B	3.025
Ba2	H9A	3.026
Ba2	H51A	3.077
Ba2	H51A	3.328
Ba2	H8B	3.338
Ba2	H53B	3.353
Ba2	H10A	3.446

2.2. *Calculations on $Ba[H_4C_4O_{10}][H_3C_4O_{10}][H_2CO_3][HCO_3]$*

We used the p, V-data from the v.d.W. corrected DFT-calculations to obtain the theoretical bulk modulus of $Ba[H_4C_4O_{10}][H_3C_4O_{10}][H_2CO_3][HCO_3]$. A 3rd-order Birch-Murnaghan equation of states (EoS) was fitted to unit cell volume between 0 GPa and 40 GPa using the software EOSFit7-GUI (Fig. S 4).[28–30] The experimentally obtained unit cell volume from the single crystal structure refinements at 40(3) GPa is shown for comparison and matches the theoretical data.

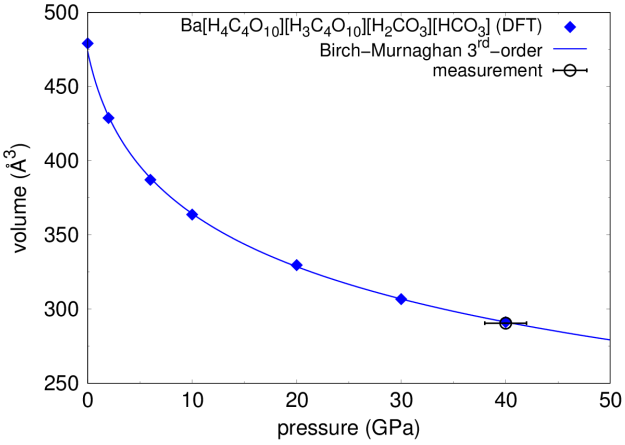

Figure S 4: Birch-Murnaghan EOS fitted to the unit cell volume of $Ba[H_4C_4O_{10}][H_3C_4O_{10}][H_2CO_3][HCO_3]$ between 0 GPa and 40 GPa obtained by DFT-based calculations in comparison to the experimental data at 40(3) GPa.

The theoretical bulk modulus is very low and shows a large pressure dependence ($K_0 = 14(2)$ GPa with $K_p = 8.2(8)$). K_0 is significantly smaller than the corresponding values for other sp^3-carbonates containing $[C_4O_{10}]^{4-}$-groups as building block such as CaC_2O_5-$I\bar{4}2$ ($K_0 = 93.4(3)$ GPa with $K_p = 4.83(2)$), which was obtained at similar conditions.[31] A high K_p-value has also be observed for other layered compounds such as graphite ($K_0 = 33.8(3)$ GPa with $K_p = 8.9(1)$) which also shows a very anisotropic compression behavior along two different directions.[32]

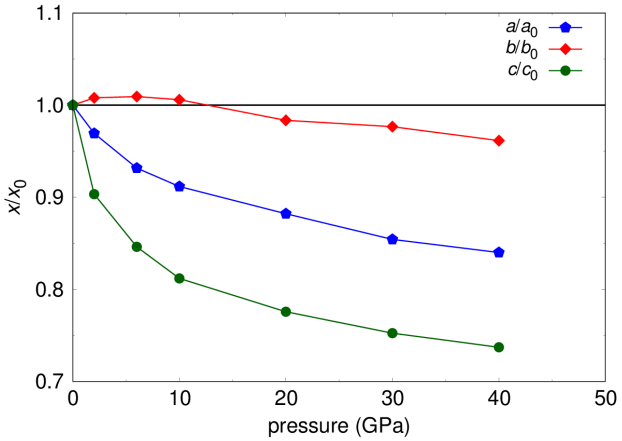

Figure S 5: Relative change of the x/x_0 ratio of the *a*-, *b*- and *c*-axes in $Ba[H_4C_4O_{10}][H_3C_4O_{10}][H_2CO_3][HCO_3]$ between 0 GPa and 40 GPa obtained by DFT-based calculations.

From the v.d.W. corrected DFT-calculations we derived a very anisotropic compression behavior of the crystal structure (Fig. S 5). We found that the structure is highly compressible along the *c*-axis ($\approx$ 25% between 0–40 GPa). This is caused by the reduction of the space between the alternating layers of the $[H_4C_4O_{10}]$-/$[H_3C_4O_{10}]^-$-groups and $[H_2CO_3]$-/$[HCO_3]^-$-groups. In contrast, within the layers the compressibility is significantly lower in the same pressure range ($\approx$ 5% along the *b*-axis).

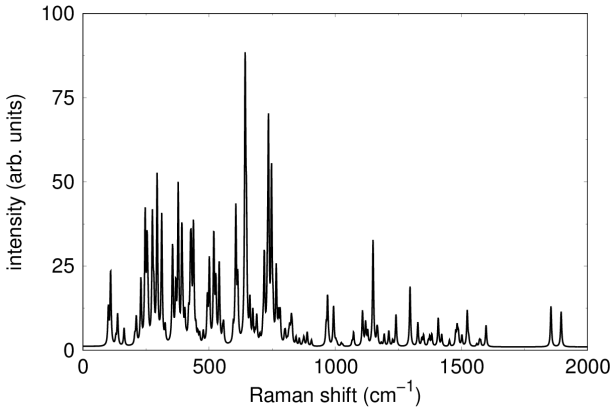

Figure S 6: DFT calculated Raman spectrum with v.d.W-correction of $Ba[H_4C_4O_{10}][H_3C_4O_{10}][H_2CO_3][HCO_3]$ at 40 GPa.

We used the v.d.W. corrected DFT-calculations to obtain the lattice dynamics at the Γ-point. Figure S 6 shows the theoretical Raman spectrum ("option 1") of $Ba[H_4C_4O_{10}][H_3C_4O_{10}][H_2CO_3][HCO_3]$ at 40 GPa.

References

(1) Pan, Y.; Wu, M.; Su, Q. Synthesis of Eu^{3+}-doped calcium and strontium carbonate phosphors at room temperature. *Mater. Res. Bull.* **2003**, *38*, 1537–1544, DOI: 10.1016/S0025-5408(03)00174-0

(2) Boehler, R. New diamond cell for single–crystal X-ray diffraction. *Rev. Sci. Instrum.* **2006**, *77*, 115103–1–115103–3, DOI: 10.1029/JB091iB05p04673

(3) Yoo, C. S.; Cynn, H.; Gygi, F.; Galli, G.; Iota, V.; Nicol, M.; Carlson, S.; Häusermann, D.; Mailhiot, C. Crystal Structure of Carbon Dioxide at High Pressure: "Superhard" Polymeric Carbon Dioxide. *Phys. Rev. Lett.* **1999**, *83*, 5527–5530, DOI: 10.1103/PhysRevLett.83.5527

(4) Mao, H. K.; Xu, J.; Bell, P. M. Calibration of the ruby pressure gauge to 800 kbar under quasi-hydrostatic conditions. *J. Geophys. Res.* **1986**, *91*, 4673–4676, DOI: 10.1029/JB091iB05p04673

(5) Spahr, D.; König, J.; Bayarjargal, L.; Luchitskaia, R.; Milman, V.; Perlov, A.; Liermann, H.-P.; Winkler, B.; Synthesis and Structure of $Pb[C_2O_5]$: An Inorganic Pyrocarbonate Salt. *Inorg. Chem.* **2022**, *61*, 9855–9859, DOI: 10.1021/acs.inorgchem.2c01507

(6) Scelta, D.; Ceppatelli, M.; Ballerini, R.; Hajeb, A.; Peruzzini, M.; Bini, R. Sprayloading: A cryogenic deposition method for diamond anvil cell. *Rev. Sci. Instrum.* **2018**, *89*, 053903, DOI: 10.1063/1.5011286

(7) Bayarjargal, L.; Fruhner, C.-J.; Schrodt, N.; Winkler, B. $CaCO_3$ phase diagram studied with Raman spectroscopy at pressures up to 50 GPa and high temperatures and DFT modeling. *Phys. Earth Planet. Inter.* **2018**, *281*, 31–45, DOI: 10.1016/j.pepi.2018.05.002

(8) Benedetti, L. R.; Loubeyre, P. Temperature gradients, wavelength-dependent emissivity, and accuracy of high and very-high temperatures measured in the laser-heated diamond cell. *High Press. Res.* **2004**, *24*, 423–455, DOI: 10.1080/08957950412331331718

(9) Du, Z.; Amulele, G.; Benedetti, L. R.; Lee, K. K. M. Mapping temperatures and temperature gradients during flash heating in a diamond-anvil cell. *Rev. Sci. Instrum.* **2013**, *84*, 075111, DOI: 10.1063/1.4813704

(10) Liermann, H.-P.; Konôpková, Z.; Morgenroth, W.; Glazyrin, K.; Bednarčik, J.; McBride, E. E.; Petitgirard, S.; Delitz, J. T.; Wendt, M.; Bican, Y.; Ehnes, A.; Schwark, I.; Rothkirch, A.; Tischer, M.; Heuer, J.; Schulte-Schrepping, H.; Kracht, T.; Franz, H. The Extreme Conditions Beamline P02.2 and the Extreme Conditions Science Infrastructure at PETRAIII. *J. Synchrotron Radiat.* **2014**, *22*, 908–924, DOI: 10.1107/S1600577515005937

(11) Prescher, C.; Prakapenka, V. B. *DIOPTAS*: a program for reduction of two-dimensional X-ray diffraction data and data exploration. *High. Press. Res.* **2015**, *35*, 223–230, DOI: 10.1080/08957959.2015.1059835

(12) Agilent, CrysAlis PRO, Yarnton, England, **2014**

(13) Aslandukov, A.; Aslandukov, M.; Dubrovinskaia, N.; Dubrovinsky, L. *Domain Auto Finder* (*DAFi*) program: the analysis of single-crystal X-ray diffraction data from polycrystalline sample. *J. Appl. Cryst.* **2022**, *55*, 1383–1391, DOI: 10.1107/S1600576722008081

(14) Dolomanov, O. V.; Bourhis, L. J.; Gildea, R. J.; Howard, J. A. K.; Puschmann, H. *OLEX2*: a complete structure solution, refinement and analysis program. *J. Appl. Cryst.* **2009**, *42*, 339–341, DOI: 10.1107/S0021889808042726

(15) Sheldrick, G. M. *SHELXT* — Integrated space-group and crystal-structure determination. *Acta. Cryst.* **2015**, *A71*, 3–8, DOI: 10.1107/S2053273314026370

(16) Sheldrick, G. M. Crystal structure refinement with *SHELXL*. *Acta. Cryst.* **2015**, *C71*, 3–8, DOI: 10.1107/S2053229614024218

(17) Hohenberg, P.; Kohn, W. Inhomogeneous Electron Gas. *Phys. Rev.* **1967**, *136*, B864–B871, DOI: 10.1103/PhysRev.136.B864

(18) Perdew, J. P.; Burke, K.; Ernzerhof, M. Generalized Gradient Approximation Made Simple. *Phys. Rev. Lett.* **1996**, *77*, 3865–3868, DOI: 10.1103/PhysRevLett.77.3865

(19) Clark, S. J.; Segall, M. D.; Pickard, C. J.; Hasnip, P. J.; Probert, M. I. J.; Refson, K.; Payne, M. C. First principles methods using CASTEP. *Z. Kristallogr.* **2005**, *220*, 567–570, DOI: 10.1524/zkri.220.5.567.65075

(20) Lejaeghere, K.; Bihlmayer, G.; Björkman, T.; Blaha, P.; Blügel, S.; Blum, V.; Caliste, D.; Castelli, I. E.; Clark, S. J.; Dal Corso, A. et al. Reproducibility in density functional theory calculations of solids. *Science* **2016**, *351*, aad3000, DOI: 10.1126/science.aad3000

(21) Monkhorst, H. J.; Pack, J. D. Special points for Brillouin-zone integrations. *Phys. Rev. B* **1976**, *13*, 5188–5192, DOI: 10.1103/PhysRevB.13.5188

(22) Baroni, S.; de Gironcoli, S.; Dal Corso, A.; Giannozzi, P. Phonons and related crystal properties from density-functional perturbation theory. *Rev. Mod. Phys.* **2001**, *73*, 515–562, DOI: 10.1103/RevModPhys.73.515

(23) Refson, K.; Tulip, P. R.; Clark, S. J. Variational density-functional perturbation theory for dielectrics and lattice dynamics. *Phys. Rev. B* **2006**, *73*, 155114, DOI: 10.1103/PhysRevB.73.155114

(24) Miwa, K. Prediction of Raman spectra with ultrasoft pseudopotentials. *Phys. Rev. B* **2011**, *84*, 094304, DOI: 10.1103/PhysRevB.84.094304

(25) Tkatchenko, A.; Scheffler, M. Accurate Molecular Van Der Waals Interactions from Ground-State Electron Density and Free-Atom Reference Data. *Phys. Rev. Lett.* **2009**, *102*, 073005, DOI: 10.1103/PhysRevLett.102.073005

(26) Spek, A. L. Single-crystal structure validation with the program *PLATON*. *J. Appl. Cryst.* **2003**, *36*, 7–13, DOI: 10.1107/S0021889802022112

(27) Murnaghan, F. The Compressibility of Media under Extreme Pressures. *Proc. Natl. Acad. Sci.* **1944**, *30*, 244–247, DOI: 10.1073/pnas.30.9.244

(28) Milman, V.; Winkler, B. Prediction of hydrogen positions in complex structures. *Z. Kristallogr.* **2001**, *216*, 99–104, DOI: 10.1524/zkri.216.2.99.20333

(29) Birch, F. Finite Elastic Strain of Cubic Crystals. *Phys. Rev.* **1947**, *71*, 809–824, DOI: 10.1103/PhysRev.71.809

(30) Gonzalez-Platas, J.; Alvaro, M.; Nestola, F.; Angel, R. *EosFit7-GUI*: a new graphical user interface for equation of state calculations, analyses and teaching. *J. Appl. Cryst.* **2016**, *49*, 1377–1382, DOI: 10.1107/S1600576716008050

(31) König, J.; Spahr, D.; Bayarjargal, L.; Gavryushkin, P. N.; Milman, V.; Liermann, H.-P.; Winkler, B. Novel calcium sp^3-carbonate CaC_2O_5-$I\bar{4}2d$ may be a carbon host in Earth's lower mantle. *Earth. Space. Chem.* **2022**, *6*, 73–80, DOI: 10.1021/acsearthspacechem.1c00284

(32) Hanfland, M.; Beister, H.; Syassen, K. Graphite under pressure: Equation of state and first-order Raman modes. *Phys. Rev. B* **1989**, *39*, 12598, DOI: 10.1103/PhysRevB.39.12598